Supplementary materials

1. Methodology

1.1 Spectroscopy, electron probe, and imaging:

Electron probe WDS analyses of florencite were undertaken using a Cameca 'microbeam' electron probe operating at 25 keV with a beam current of 30nA and a 5 micron spot size. REE peaks were calibrated to synthetic REE phosphate standards.

Electron probe EDS analyses were undertaken using the Research School of Earth Sciences (RSES), Australian National University (ANU) Cameca electron probe and a JEOL 6400 scanning electron microscope at the Electron Microscopy Unit, Australian National University (ANU). Backscattered electron images were produced with the JEOL 6400 SEM at the Electron Microscopy Unit.

To determine the relationship of the pore minerals to the carbonado, Pb isotopic measurements were done on large florencite minerals found in the pores of two CAR carbonados. CAR carbonados were chosen because, unlike the Brazilian carbonados, the electron probe analyses showed that the florencite in the CAR carbonados had a significant plumbogummitic substitution. As a result, they generally contained 0.5%-2% Pb. The Pb isotopic ratios were analyzed in situ with the SHRIMP II ion microprobe at RSES prior to the addition of a multicollector. The isotopes measured were ^{204}Pb, ^{206}Pb, ^{207}Pb, ^{208}Pb and $^{208}Pb^{1}H$. This last species, with a nominal mass of 209, was measured because florencite is a hydrous mineral, and the hydride PbH was expected to be produced. The ratio of ^{208}Pb to $^{208}Pb^{1}H$ was used to determine the hydride correction, which was then applied to the other isotopes. In most cases, the $^{208}Pb^{1}H/^{208}Pb$ ratio was about 0.2%. All mineral targets were significantly larger than the ~20 micron ion probe spot size.

Cathodoluminescence images were taken using a luminoscope for initial low magnification color images. Followup work was done with SEM.

A microscope-mounted luminoscope operating between 10 and 20 kV, and a Nuclide luminoscope with a Leitz automatic camera shooting Kodak Ektachrome 320T film were used for most cathodoluminescence pictures. Some CL images were also taken with an optronics CCD camera and luminoscope at the Smithsonian Museum of Natural History, USA. All samples were at room temperature. Between 10 and 20 kV the electron penetration distance in diamond is between 1.4 and 4.3 μm (Davies, 1979).

Polished carbonado specimens were carbon coated and imaged using a Gatan ChromaCL2 mounted on an Hitachi S3700N SEM at the Smithsonian Institution's Museum Conservation Institute. An electron beam energy of 7 keV and high vacuum conditions were employed to excite diamond luminescence. This SEM-based multispectral system disperses light via a grating, and utilizes 16 photomultiplier tubes to capture photons from 300 – 750 nm. The luminescence signal is then binned into four channels red (R), green (G), blue (B), and ultra violet. The images presented in this study represent a composite of the visible, or RGB.

Radiation-induced CL halos (Figure 1) were measured by manually fitting a circle to a halo. The mean measured diameter of 24.0 ± 1.2 mm (n=6). This result is consistent

with a calculated radius of 12 mm in diamond for 5.30 MeV alpha particles in diamond owing to the decay of ^{214}Po which is an intermediate product of ^{238}U decay.

1.2 Sample collecting

Heavy minerals separates, river sands, and rock samples were collected during a November 1998 field excursion to the Chapada Diamantina, Bahia state, Brazil. River sand was collected from rivers and diamond washing tailings from several tributaries of the Rio São Jose and the Rio Santo Antônio, as well as streams from near the former mining towns of São João and Ventura. Sands were sieved on-site, and pebbles were examined for traditional indicator minerals.

Some sand samples were concentrated on-site by a garimpeiro using a bateia, the traditional Brazilian gold-and-diamond pan. This resulted in a 100-200 g sample enriched in heavy minerals.

Rock samples from fuchsitic Jacobina quartzites were collected at roadcuts along highway BA-324 east of Jacobina town. Three separate quartzite layers from the Rio do Ouro Formation were sampled.

Tombador Formation samples were taken from outcrops along the Rio Cachorrinho, Rio Lençóis, and Rio Ribeirão, or from river boulders. The drainages of the Rio Cachorrinho is entirely underlain by Tombador formation (Figure DR1), so the probability of the clasts collected being non-Tombador boulders with similar appearance is small. This is especially true for the fuchsitic quartzite clasts, as these are only reported from the Lavras Conglomerate in the Tombador Formation (Sampaio et al., 1994).

1.3 Laser ICP-MS zircon dating

Three zircon populations were dated by laser ICP-MS using the methods described in Ballard et al. (2001). One zircon group of 100 zircons was from the green fuchsitic Jacobina quartzite. Another group of 100 zircons was from the green fuchsitic quartzite clasts in the Lavras Conglomerate of the Tombador Formation. Fifty zircons from a Rio Cachorrinho bateia concentrate comprised the third group. Zircon standards of known age were used to standardize the Pb isotopic ratios and U/Pb ratios. An AS57 standard, with an age of 1099 Ma, was used for the Jacobina and Tombador clasts. A SL13 standard with an age of 572 Ma was used for the Rio Cachorrinho samples. The glass standard used to determine U/Pb concentrations and U/Th ratios was NBS 612. The analytical procedure followed was this: 1 NBS glass, 5 Tombador, 5 Jacobina, 2 AS57, 5 Jacobina, 5 Tombador, 2 AS57.

Analysis time was 65 seconds, with 20 seconds of background collected before the Lambda Physik lpx 120i 193nm excimer laser was turned on at an operating frequency of 5 Hertz. The laser spot size was 30 μm, the average crater depth was about 45 μm. This resulted in drilling entirely through some of the smaller zircons, in which case post-drill-through data was discarded. The Agilent 7500 series inductively coupled plasma mass spectrometer counted the following masses for the times indicated: ^{29}Si, 10 ms; ^{31}P, 10 ms; ^{96}Zr, 10 ms; ^{178}Hf, 10 ms; ^{206}Pb, 150 ms; ^{207}Pb, 150 ms; ^{208}Pb, 100 ms; ^{232}Th, 25 ms; ^{238}U, 25 ms. Including switching time, this cycle was repeated every 0.6 seconds.

A zircon standard was used for all values except the U/Th ratio, which was obtained from the NIST 612 glass. This standardization procedure factors out down-hole fractionation and instrumental mass bias. The same standardization was then applied to the unknowns. Age results which were more than 5% discordant between the $^{207}Pb/^{235}U$, $^{206}Pb/^{238}U$, and $^{208}Pb/^{232}Th$ systems were considered unreliable, as were those where the observed error was more than three times the error expected from counting statistics.

1.5 SHRIMP zircon dating

The mount containing the Tombador green clast and Jacobina zircons was cut up to allow insertion of some modern reference materials and recast, with a slight repolish. The mount was a standard 25mm epoxy mount. An attempt was made to fill the laser holes with epoxy; to reduce surface topography; this was successful in about 30% of the cases. Approximately 75 Tombador and 70 Jacobina zircons were analysed along with 15 OG1 (Stern et al., 2009) and 19 Temora-2 (Black et al., 2004) reference zircons. The SHRIMP and laser grain numbers for individual zircons measured with both methods are indicated in tables DR4-7..

The analytical run table included standard uranium lead geochronology peaks: $^{90}Zr_2{}^{16}O$ reference peak, a background position, ^{204}Pb, ^{206}Pb, ^{207}Pb, ^{208}Pb, and ^{238}U. The standard actinide oxides used for U-Pb calibration (Williams, 1998) were measured: $^{232}Th^{16}O$ (248), $^{238}U^{16}O$ (254), $^{238}U^{16}O_2$ (270). Analyses were run automatically using standard Geoscience Australia procedures. A primary impact energy of 10680 Volts was used, with secondary ions initially extracted at 680 volts before acceleration to 10 kV for mass spectrometric analysis. The SHRIMP was set up with a 110 micron source slit and a 100 micron collector slit, yielding a 1% mass resolution ($M/\Delta M$) of 5000 or greater for all peaks. Data were collected in six scans through the run table on a single electron multiplier. Data were reduced using SQUID 2.5 (Ludwig, 2010). Analytical and data reduction procedures are described in detail elsewhere (Magee et al., 2012).

2. Carbonado additional textural and spectral details:

2.2.2 Reflected light textures

2.2.2.1 Anhedral texture

Figure DR2 shows the microtextures of a variety of carbonado stones. Most carbonado consists entirely of anhedral grains of diamond (Figure DR2a-e), which have irregular grain boundaries and a large grain size distribution, ranging from less than 1 mm to over 40 mm. Six of the eight carbonado samples from the CAR, and seven of the thirteen Brazilian samples exhibit only this anhedral texture. Although the average grainsize can vary, the microtexture of both Brazilian and CAR samples is similar (Figure DR2). In addition, all carbonados, with the possible exception of Brazilian samples R-F7 and L-5, exhibit an anhedral, interlocking grain texture for at least some parts of the observed polished surfaces. There are several variations to the anhedral grain texture, some of which are described below.

2.2.2.2 Increased grainsize along pore boundaries

In some cases, the grainsize of the anhedral carbonado texture increases close to pores. In addition, the grain boundaries between these larger grains tend to be less jagged and irregular than typical diamond grains in carbonado. Figure DR2c, DR2d shows an example of enlarged grain size around carbonado pores. This feature is common in grains CAR 16 and CAR 24, and it can also be seen in sample CAR 2, along with Brazilian samples R-G1 (fig. DR2e) and R-E3 (fig DR2b).

2.2.2.3 Fractures and fine-grained planes.

In addition to having enlarged grains along pore boundaries, carbonados can also have features showing reduced grainsize. Figure DR2d (CAR 24) shows a linear feature along which the diamond grainsize is reduced relative to the rest of the sample. The cause of this feature is unknown, but CL imagery suggests that this area is more porous that the rest of the carbonado, and has been damaged by radiation to a greater degree.

2.2.2.4 Intra-carbonado anhedral grain size inhomogeneity

Figure DR2a-c show that different carbonados with an anhedral microtexture can have different average grainsizes. However, one carbonado was found where the average grainsize varies across the polished surface on the single stone. Brazilian carbonado R-G1, shown in Figure DR2e, has an average grain size that is anywhere from 5 to 60 mm, depending on the area studied. The sample consists of areas of lobate coarse-grained features 100 to 500 mm in size, which are separated by regions of very small average grainsize. The origin of these features is unknown.

2.2.2.5 Euhedral microdiamonds in carbonado

Two of the CAR carbonados studied, and six of the Brazilian ones, have a texture that does not consist entirely of interlocking anhedral diamond crystals. As is shown in Figure DR2f-h, these carbonado samples have larger monocrystals imbedded in the anhedral matrix. The monocrystals are generally larger than the grains in the anhedral textured carbonados. However, the anhedral matrix is generally finer grained than that in anhedral carbonados. Euhedral monocrystals in carbonado were first observed by Fettke and Sturges (1933), and later researchers suggested that they may be an indicator of two stage growth processes (Trueb and de Wys, 1971).

2.2.2.6 Fractured monocrystals

In three of the carbonados studied, the euhedral monocrystals were fractured. Figure DR2g,2h shows and example of this, where euhedral diamond crystals with square cross- sections have been fractured. CAR-1 is also an example of a carbonado that has pores with a preferred orientation- in this picture they tend to trend from lower right to upper left. These pores have an irregular shape where they border the euhedral grains, but more rounded borders where they are surrounded by anhedral matrix.

2.2.2.7 Low matrix carbonado

In one carbonado, there is almost no matrix at all. Figure DR2h shows Brazilian carbonado R-F7. This stone has very few irregular, interlocking grains, and instead is composed mostly of polygonal grains, many of which are fractured. As in carbonado CAR-1, the grain boundaries of these monocrystals intrude into the pores, giving the pores very irregular shapes.

2.2.2.8 Other textures

Carbonado L-5, from Brazil, has very large crystals, which may exceed one mm in size. However, these crystals are fractured, and reflected light images of this carbonado do not reveal grain boundaries. CL studies show that most of the surface features seen in reflected light are intragranular fractures. Extensive studies of this sample have been published (Wilson et al., 2012).

2.3 Cathodoluminescence studies of carbonado texture

Not all CL features in carbonado are caused by radiation damage. In particular, those carbonados which contain euhedral monocrystals often exhibit CL features that reveal textural information. Even then, however, the activated centers are radiation-related defect centers whose intensity is goverened by structural features, possibly relating to N aggregation.

2.3.1 Cathodoluminescence differences between euhedral microdiamonds and anhedral matrix

The CL of the euhedral microdiamonds found in some carbonados is often strikingly different in color and intensity that that of the surrounding matrix (Magee and Taylor, 1999). However, in all carbonado studies, the same defect centers were present (Wilson et al., 2012), with differences in apparent color due to relative intensities of the different defect ceters.

3 Pore mineral Chemistry

3.2 Inclusions found in five carbonados

Inclusions from five carbonados, three from the CAR, and two from Brazil, were examined as part of this study. Compositions of the REE phosphates are reported. Abundant clay and iron oxide/hydroxide minerals were also observed, but were not studied in detail.

Carbonado has long been known to contain REE phosphates, the most common of which is florencite (Trueb and Butterman, 1969). Florencite was analysed for major element composition and Pb isotopic composition.

Florencite was found in three carbonados from the CAR and one from Brazil. Florencite compositions from two of the CAR carbonados are given in Table DR1, and the high Sr, Ba, and Pb contents indicate extensive solid solution with the crandalite series endmembers (Schwab et al., 1990).

3.2.1 Other REE phosphates

Two other REE phosphates were detected. One, a single $LaPO_4$ grain detected in sample CAR-16, may be the possible monazite previously reported (De et al., 1998). However, our results (Table DR1) show less Ce and other heavier REEs than were reported by De et al.(1998). The low totals found in this case suggest that it may be a hydrated light rare earth phosphate, such as rhabdophane.

The other REE phosphate, a hydrated YPO_4 mineral found in samples CAR-16 and B2, is probably the churchite described by Trueb and de Wys (1971). No WDS spectra were taken of this mineral, and neither of these phases contained abundant lead.

3.3 Isotopic ratio of florencite Pb

The significance of the pore minerals, and in particular, the REE phosphates, to carbonado genesis, is not well known. To constrain their relative ages, the lead isotopic composition of the florencite in samples CAR-16 and CAR-2 was measured. The florencite in both of these samples had a Pb content of between 2% and 7% , presumably in the form of a plumbogummitic solid solution ($PbAl_3(PO_4)(HPO_4)(OH)_6$). The % levels of Pb make in-situ Pb isotopic analysis practical using the SHRIMP II ion probe. The results are shown in Table DR2, below.

3.4 Discussion of pore minerals

Carbonado is not the only diamond that contains epigenetic, REE-bearing, hydrated phosphates. Gorshkov et al. (1997) also reported an epigenetic florencite inclusion in diamond with Ba, Ca, Sr, Pb crandalite series components similar to that reported in section 3.2.

The measured florencite compositions are not exactly stochiometric, but they are within reported deviations for both natural and synthetic crandalites (Schwab et al., 1990). These compositions are broadly similar to those reported by (De et al., 1998), except that Pb was detected as a plumbogummite component in the florencite.

Bulk carbonado contains two lead isotopic populations (Ozima and Tatsumoto, 1997). The first of these is a modern common Pb component, which can be removed from the carbonado by intense acid leaching.

Because the Pb in florencite is modern and common, this mineral most likely formed in the placer deposits from which carbonado is mined. The similarity between the results of this study and the leached Pb previously reported (Ozima and Tatsumoto, 1997), suggests that florencite is the source for the lead leached from carbonado studied by Ozima and Tatsumoto (1997). The source of the radiogenic component can be constrained by studying radiation damage of carbonado.

4 Radiation damage

4.1 Previous studies of Radiation Damage

There is considerable evidence that carbonado has been subjected to high levels of ionizing radiation (Ozima et al., 1991; Ozima and Tatsumoto, 1997; Milledge et al., 1998; Shelkov et al., 1998). The detection of noble gas isotopic signatures characteristic of spontaneous ^{238}U fission suggests that this radiation damage was caused by U (Ozima et

al., 1991). In addition, Milledge et al. (1998) report radiation halos in carbonado that correspond to U, not Th decay.

4.2 Cathodoluminescence evidence for radiation damage

Radiation damage in diamond can be detected with cathodoluminescence (CL), because ionizing radiation causes damage to the crystal structure of diamond. This damage gives rise to optical centers that luminescence at different frequencies than color centers that are unrelated to radiation damage. Severe irradiation will quench these optical centers, so that severely damaged diamond does not luminesce, and appears dark in CL images.

4.2.1 CL spectra

The CL spectra generally showed the same defects reported previously in carbonado (Wilson et al., 2012). No differences between African or Brazilian samples were observed.

4.2.2 Bull's eye features

Figure 1 (main text) is a multispectral SEM cathodoluminescence image of CA carbonado R-G1, which shows well-developed radiation halos formed by point source radiation damage (Mendelssohn et al., 1979). Both light and dark halos are present, and in many cases, the bright halos are orange, while the surrounding carbonado has a green CL response.

Thirteen of the 21 carbonado specimens studied exhibit bulls-eye halos. Similar features are visible in carbonado from the CAR, and are shown in Figure DR3. More often, these halos are in the form of a single dark ring, 20 to 25 μm in diameter, and the multi-ring pattern is not visible.

The concentric circles of radiation damage (fig. S3-S7) are caused by alpha particle damage to the diamond structure. Because the alpha particles released at different steps in the U or Th decay sequence have different characteristic energies, different radionuclides give rise to different halo patterns (Mendelssohn et al., 1979). Although the halos in carbonado are generally not well preserved enough to accurately determine which nuclide formed them, the 31 μm radius ^{212}Po decay ring characteristic of the Th decay series does not appear in halos found in carbonado. In addition, all of those halos that are preserved well enough to show multiple rings show the double or triple ringed pattern characteristic of U, not the 4-5 ring pattern caused by Th. This supports the identification made by Milledge et al. (1998), who state that the halos are formed by U, not Th..

Because carbonado is known to contain numerous REE phases (see section 2.1.2), the possibility that these halos are from alpha decay of ^{147}Sm should be considered, since some of the florencite in these carbonados contain as much as 0.6% Sm_2O_3. However, the alpha particle generated by ^{147}Sm decay has an energy of only 2.3 MeV, far less than that of any of the decay steps in the Th or U series. As a result, it would have a penetration distance of less than 5 μm, and thus can not be responsible for a 20 μm radius halo.

4.2.3 Pore Halos

Radiation damage halos in carbonado are not limited to point sources. In fact, the most prevalent radiation damage features in carbonado are associated with pores. These can take the form of a change in CL color, a change in intensity, or most often, a complete CL quench, (Figure DR3, DR4). Pore halos are often associated with Bull's eye halos. In some cases, small pores seem to have halos intermediate between the dark pore halos and the bull's eye halos that are a result of point radiation sources (Figure DR5, S6).

Pore halos usually extend 20-25 microns from the pore edge, a distance which is similar to the alpha penetration distance in diamond from U series decay (depending on the shape of the pore in 3d). This suggests that the pores of carbonado contained a U-bearing phase, and alpha particles from U decay penetrated the diamond surrounding these pores, producing the lattice defects responsible for the observed CL features. Most of these pores are now empty, but some contain florencite, clays, or other lateritic minerals. Further evidence supporting radiation damage as the cause of these dark halos is presented in the Raman section (5).

Ozima et al. (1991) shows that fissionogenic Xe, Kr, and He from alpha decay have been implanted in the diamond lattice. These CL images suggest that the primary areas where this has occurred are the CL dark halos that are mainly found surrounding carbonado pores. The exterior of carbonados are also often dark in CL, suggesting that radiation damage may also have come from outside the carbonado.

4.2.4 Channels

Although the features described previously show that carbonado has been effected by radiation damage from uranium decay, and that the radioactive material responsible was contained in the pores or in point sources along grain boundaries. These features do not show how the U got there, or what has since happened to it. Because U in its most oxidized valence state (6^+) is soluble as $(UO_2)^{2+}$(or various uranyl complexes such as $UO_2(SO_4)^0$ depending on chemical environment), it would be reasonable to suspect aqueous transport as a potential mechanism for emplacing and removing the uranium. Luminescence features that have the appearance of channelways are present in some carbonados. Previous studies have shown a network of interconnecting lines of darkened CL response that connect with pores (Magee and Taylor, 1999). A few of these lines are decorated with bull's eye halos, suggesting radioactive materials were deposited in these channels. The association of bull's eye halos with cracks was also noted by Milledge et al. (1998) in one of the carbonados described in that study. Three of 21 carbonados in this study showed flow channel features.

4.2.5 Radiation damage along cracks

One of the specimens retrieved during the field excursion to Bahia, Brazil, L-5, shows a very different textural and luminescence pattern compared with the other 20 carbonados studied (Figure DR7). The most unusual feature of this diamond is its extremely large crystal size, and the preservation of what appear to be original CL features, which in some parts of the stone are not affected by later radiation damage. In other parts of the stone, these original features are overprinted by radiation-induced CL associated with

pores and cracks (Figure DR7). The crack-related radiation damage produces both green and orange CL responses. Four carbonados show radiation damage along cracks. Hyperspectral imaging of this specimen drew similar conclusions (Wilson et al., 2012).

4.3 Implication for 'glassy' surfaces

Figure DR8 shows the exterior of carbonado CAR 1. The unusual exterior textures have been previously described as deriving from a "highly unequilibrated process" (Shelkov et al., 1998) or being "melt-like" (Haggerty, 2014). In contrast to these strange textures, carbonado CAR 24 has rounded, frosted corners and edges, suggesting that this carbonado was abraded in a high energy sedimentary environment (Figure DR9). However, as is shown in Figure DR9, the exterior pores of this carbonado still retain the shiny black texture shown on the exterior of carbonado CAR 1 in Figure DR8. This texture also seems to be present in the interior pores, although the presence of pore minerals and the brightness of the polished diamond surface in reflected light make photographing this effect difficult. The presence of this texture in pores, its "glassy" appearance, and the difficulty obtaining Raman spectra from carbonado exteriors and near-pore grains, suggest that this texture may be the result of severe radiation damage to diamond by radioactive minerals previously present in the pores and on the exterior of carbonado.

5 Raman and Photoluminescence

5.3.1 Previous work

Photoluminescence (PL) and Raman spectroscopy also provide crystallographic information on carbonado. Raman spectra of carbonado exteriors were measured by Knight and White (1989). These showed that the peak width in carbonado is about 50% wider than in synthetic or natural monocrystalline diamond, but 5-10 times narrower than peak widths in CVD or meteoritic (ureilite) diamonds, and much narrower than the Raman bands of impact produced diamonds (Knight and White, 1989; Miyamoto et al., 1993) (Knight and White, 1989; Miyamoto et al., 1993). Further work (Fukura et al., 2005; Kagi and Fukura, 2008) suggests up to 0.7 GPa of internal stress are present in CAR carbonado.

5.3.2 PL interference with Raman

Raman and PL are both generated by illumination with monochromatic light. This can cause interference between the Raman and the PL, as was previously reported in carbonado (Kagi et al., 1994), where it was shown that the PL response often interfered with the detection of the Raman peak. Only three of the carbonados studied, CAR 24, CAR 17, and B-1, had Raman bands that could be measured.

5.3.3 Raman spectroscopy of a radiation damage halo

In order to determine whether any detectable change occurs in the Raman close to pores surrounded by CL dark halos, Raman spectra were taken from carbonado B-1 at intervals along a transect moving away from the pore. Carbonado B-1 was chosen because it has relatively dim PL, and there was little or no PL interference with the Raman bands for this set of measurements. As previously reported (Magee and Taylor,

1999) the closer the measurement was to the pore, the wider and less intense the Raman band was. All of the bands from areas of the carbonado inside of the halo are broader and less intense than the one from the spot farthest from the pore, and just beyond the edge of the CL dark halo.

These measurements are consistent with increasing pore-wards crystal lattice damage resulting from a radiation source located in the pores which emitted energetic particles with a penetration distance of approximately 25 microns. This is similar to the penetration distance for uranium-related alpha particles and fission decay products in diamond (Daulton and Ozima, 1996; Mendelssohn et al., 1979).

5.3.4. Lack of Raman spectra for non-diamond carbon species

Raman spectroscopy is used by material scientists to detect non-diamond carbon species in synthetic diamond, especially CVD diamond. This is because most other forms of carbon give a Raman response that is many times more intense than that of diamond, so that only a tiny amount of non-diamond carbon will be easily detectable using Raman spectroscopy (Knight and White, 1989). Despite the assertion that the black color of carbonado is due to the presence of graphite or amorphous carbon (Kagi et al., 1994; Trueb and Butterman, 1969), no Raman lines for lonsdaleite, graphite, or amorphous carbon were detected in any of the carbonados studied.

However, there are some areas of carbonado that give no Raman or PL response at all (Magee and Taylor, 1999). Severely damaged areas of both CAR and Brazilian carbonado showed a featureless, dark luminescence spectra from near cores or external surfaces, which we interpret as radiation-induced amorphitization.

5.3.5. Identification of photoluminescence lines

The photoluminescence spectra observed were generally similar to those seen previously (Fukura et al., 2005; Kagi and Fukura, 2008) and correspond to the same defects observed in CL (Rondeau et al., 2008; Sautter et al., 2011; Wilson et al., 2012). The same defects were observed in all CAR and Brazilian carbonado in this study.

6.2.2 Laser ICPMS U/Pb Age of detrital zircons from the Rio Cachorrinho

Fifty zircons from the Rio Cachorrinho were dated using laser ablation ICP-MS, to determine how the whole-stream zircon population compared to that of the conglomerate clasts of the formation through which the stream ran. The results of these analyses are shown in Table DR3 and Figure DR10. Most of these ages are on or near concordia, although the few analyses that are less than 5% discordant were discarded. Ten more have high experimental errors, and suggest mixed ages. These have also been discarded. The remaining 37 grains are plotted on the frequency distribution diagram shown in Figure DR11.

6.2.3 U/Pb Age of detrital zircons from green quartz clasts in Tombador conglomerate

The zircon sample extracted from the green quartzite clasts of the Tombador Formation conglomerate consisted mostly of well rounded, frosted, grains. Only 8% of the population retained relict crystal shapes in the form of partial or subrounded pyramidal terminations. Almost 50% of the grains were broken. The aspect ratio of the Tombador grains ranged from 1.1:1 to 2.5:1, but most grains were between 1.25:1 and 1.75:1. These zircons were generally dark reddish-brown or purple in color. About 50% of the population was opaque, or at least too dark for the color to be apparent in transmitted light observations of the grain mount.

The average grain size was about 162 μm by 99 μm. Cathodoluminescence images revealed that although a few of these grains were intensely zoned, most were CL dark. The CL dark grains were usually strongly colored. Often the center of the zoning was not in the center of the grain. This observation, and the number of broken grains, suggests that many of these zircons are fragments.

6.2.3.1 Pb loss event

The U and Pb isotopic ratios of the studied grains are shown in Table DR4 and Figure DR12. Almost all of the grains exhibit some degree of lead loss, which in some cases was almost total. This Pb loss seems to have occurred at 0.367 ± 0.054 Ga. No regional geologic event is known to have occurred at this time, but conventional U/Pb data (Mougeot, 1996) also show Pb loss in the late Paleozoic. Previous SHRIMP U/Pb data (Nutman and Cordani, 1993; Nutman et al., 1994) show a similar trend in zircon from the Contendas-Mirante rocks, but this lead loss is interpreted as a 0.6 Ga Pan-African lead loss event. Discordance is calculated using the SQUID 2 formula (Ludwig (2010) for consistency with the SHRIMP data. Ages more than 5% discordant have not considered when discussing these results. This results in a concordant sample size of 31.

6.2.4 U/Pb age of detrital zircons from the Jacobina quartzite

The zircon sample extracted from the Jacobina quartzite consisted mostly of well rounded, frosted, slightly elongated grains. Approximately 17% of the population retained relict crystal shapes in the form of partial or subrounded pyramidal terminations. About 20% of the grains were broken. The aspect ratio of the Jacobina grains ranged from 1.2:1 to 3.4:1, but most grains were between 1.5:1 and 2:1. Optically, these zircons were generally colorless to light brown, although a few darker, purple grains were present. About 17% of the population was opaque.

The average grain size was about 103 μm by 78 μm. CL images revealed that many of these grains are intensely zoned. In less than 40% of the grains is the center of the zonation pattern located in the center of the grain, indicating that sedimentary rounding has affected most of the grains, or broken them into fragments that were then further rounded. CL intensity varies greatly, with optically dark grains generally being CL dark. The U and Pb isotopic ratios of the studied grains are shown in Table DR5 and Figure DR13.

6.2.4.1 Pb loss event

Almost all of the grains exhibit some degree of lead loss, which is some cases was almost total. This Pb loss seems to have occurred at 0.383 ± 0.11 Ga, and is within error of the Tombador Pb loss and other regional studies (Mougeot, 1996; Nutman et al., 1994). Discordance is calculated using the SQUID 2 formula (Ludwig (2010) for consistency with the SHRIMP data. Only those grains that were 95% concordant were used. This resulted in a sample size of 53.

6.3 SHRIMP data

In a single analytical session on the Geoscience Australia SHRIMP IIe, 19 Temora II reference zircons, 15 OG1 reference zircons, a 91500 concentration reference material, 71 Jacobina zircons, and 75 of the green clast Tombador zircons were analysed. Unknowns were targeted using a customized prototype of the Geostar (Norris Software) laser ablation control software, which was modified to sync with the SHRIMP autoanalysis software. The individual zircon grain numbers do not correspond in all cases, and individual zircons dated by both methods are indicated in Tables S4-7. The 19 Temora analyses had a 0.28% internal reproducibility, with a MSWD of 1.25 and a 0.21 probability of fit. The 15 OG1 analyses had a weighted mean $^{207}Pb/^{206}Pb$ age of 3.4681 ± 0.0031 Ga, with a MSWD of 0.53 and a probability of fit of 0.92. This value is within error of the reference value (Stern et al., 2009).

6.3.1 Tombador data

The SHRIMP Tombador data (Table DR6, Figure DR12) were generally consistent with the LA-ICPMS data, with a precision that was generally 1.5 to 2 times better on a per-spot basis. Thirty-two of the 70 analyses were less than 5% discordant. The oldest zircon was confirmed with an age of between 3.69 and 3.70 Ga. The youngest population was ~3.34 Ga. See text for discussion.

6.3.2 Jacobina data

The SHRIMP Jacobina data (Table DR7, Figure DR13) were similar to the laser ICP data, with the advantage that concordant regions were found on several older zircons that were 5-15% discordant for the laser analyses. Fifty-five of the 71 analyses were less than 5% discordant. This yielded an oldest grain of 3.65 Ga. The youngest population comprising ~31 zircons has a well-defined age of 3.308 ± 0.003 Ga (95% confidence interval). See text for discussion.

References:

Ballard, J.R., Palin, J.M., Williams, I.S., Campbell, I.H., and Faunes, A., 2001, Two ages of porphyry intrusion resolved for the super-giant Chuquicamata copper deposit of northern Chile by ELA-ICP-MS and SHRIMP: Geology, v. 29, no. 5, p. 383–386.

Black, L.P., Kamo, S.L., Allen, C.M., Davis, D.W., Aleinikoff, J.N., Valley, J.W., Mundil, R., Campbell, I.H., Korsch, R.J., Williams, I.S., and Foudoulis, C., 2004, Improved $^{206}Pb/238U$ microprobe geochronology by the monitoring of a trace-

element-related matrix effect; SHRIMP, ID–TIMS, ELA–ICP–MS and oxygen isotope documentation for a series of zircon standards: Chemical Geology, v. 205, no. 1–2, p. 115–140.

Daulton, T.L., and Ozima, M., 1996, Radiation-Induced Diamond Formation in Uranium-Rich Carbonaceous Materials: Science, v. 271, no. 5253, p. 1260–1263.

Davies, G., 1979, Cathodoluminescence, *in* Field, J.E. ed., Properties of Diamond, Academic Press, London, p. 165–181.

De, S., Heaney, P.J., Hargraves, R.B., Vicenzi, E.P., and Taylor, P.T., 1998, Microstructural observations of polycrystalline diamond: a contribution to the carbonado conundrum: Earth and Planetary Science Letters, v. 164, no. 3–4, p. 421–433.

Fettke, C.R., and Sturges, F.C., 1933, Structure of carbonado or black diamond: American Mineralogist, v. 18, p. 172–174.

Fukura, S., Nakagawa, T., and Kagi, H., 2005, High spatial resolution photoluminescence and Raman spectroscopic measurements of a natural polycrystalline diamond, carbonado: Diamond and Related Materials, v. 14, no. 11–12, p. 1950–1954.

Gorshkov, A.I., Bao, Y.N., Bershov, L.V., Ryabchikov, I.D., Sivtsov, A.V., and Lapina, M.I., 1997, Inclusions of native metals and other minerals in diamond from kimberlite pipe 50, Liaoning, China: Geochemistry International, v. 35, p. 695–703.

Haggerty, S.E., 2014, Carbonado: Physical and chemical properties, a critical evaluation of proposed origins, and a revised genetic model: Earth-Science Reviews, v. 130, p. 49–72.

Kagi, H., and Fukura, S., 2008, Infrared and Raman spectroscopic observations of Central African carbonado and implications for its origin: European Journal of Mineralogy, v. 20, no. 3, p. 387–393.

Kagi, H., Takahashi, K., Hidaka, H., and Masuda, A., 1994, Chemical properties of Central African carbonado and its genetic implications: Geochimica et Cosmochimica Acta, v. 58, no. 12, p. 2629–2638.

Knight, D.S., and White, W.B., 1989, Characterization of diamond films by Raman spectroscopy: Journal of Materials Research, v. 4, no. 2, p. 385–393.

Ludwig, K., 2010, SQUID 2: a user’s manual:

Magee, C.W., and Taylor, W.R., 1999, Constraints from Luminescence on the History and Origin of Carbonado.: Proceedings of the Viith International Kimberlite Conference., v. 2, p. 529–532.

Magee, C.W., Withnall, I.W., Hutton, L.J., Perkins, W.G., Donchak, P.J.T., Parsons, A., Blake, P.R., Sweet, I.P., and Carson, C.J., 2012, Joint GSQ–GA geochronology project, Mount Isa Region, 2008–2009:

Mendelssohn, M.J., Milledge, H.J., Vance, E.R., Nave, E., and Woods, P.A., 1979, Internal Radioactive Haloes in Diamond: Diamond Research, p. 31–36.

Milledge, H.J., Woods, P.A., Beard, A.D., Shelkov, D.A., and Willis, P., 1998, Cathodoluminescence of Polished carbonado: 7th International Kimberlite Conference extended abstracts, p. 589–590.

Miyamoto, M., Takase, T., and Mitsuda, Y., 1993, Raman spectra of various diamonds: Mineralogical Journal, v. 16, no. 5, p. 246–257.

Mougeot, R., 1996, Etude de la limite Archeen-Proterozoique et des Mineralisations Au, +/- U Associees: Universite Montpellier II, Montpellier.

Nutman, A.P., and Cordani, U.G., 1993, SHRIMP U-Pb zircon geochronology of Archaean granitoids from the Contendas-Mirante area of the São Francisco Craton, Bahia, Brazil: Precambrian Research, v. 63, no. 3–4, p. 179–188.

Nutman, A.P., Cordani, U.G., and Sabaté, P., 1994, SHRIMP U-Pb ages of detrital zircons from the early proterozoic Contendas-Mirante supracrustal belt, São Francisco Craton, Bahia, Brazil: Journal of South American Earth Sciences, v. 7, no. 2, p. 109–114.

Ozima, M., and Tatsumoto, M., 1997, Radiation-induced diamond crystallization: Origin of carbonados and its implications on meteorite nano-diamonds: Geochimica et Cosmochimica Acta, v. 61, no. 2, p. 369–376.

Ozima, M., Zashu, S., Tomura, K., and Matsuhisa, Y., 1991, Constraints from noble-gas contents on the origin of carbonado diamonds: Nature, v. 351, no. 6326, p. 472–474.

Rondeau, B., Sautter, V., and Barjon, J., 2008, New columnar texture of carbonado: Cathodoluminescence study: Diamond and Related Materials, v. 17, no. 11, p. 1897–1901.

Sampaio, D.R., da Costa, E.D.A., and Neto, M.C.A., 1994, Diamantes e carbonados do alto Rio Paraguaçu: geologia e potencialidade econômica: CPBM.

Sautter, V., Lorand, J.-P., Cordier, P., Rondeau, B., Leroux, H., Ferraris, C., and Pont, S., 2011, Petrogenesis of mineral micro-inclusions in an uncommon carbonado: European Journal of Mineralogy, v. 23, no. 5, p. 721–729.

Schwab, R.G., Herold, H., Gotz, C., and De Oliveira, N.P., 1990, Compounds of the crandallite type: synthesis and properties of pure rare earth element-phosphates: Neues Jahrbuch für Mineralogie Monatshefte, , no. 6, p. 241–254.

Shelkov, D.A., Verchovsky, A.B., Milledge, H.J., and Pillinger, C.T., 1998, The radial distribution of implanted and trapped 4He in single diamond crystals and implications for the origin of carbonado: Chemical Geology, v. 149, no. 1–2, p. 109–116.

Stern, R.A., Bodorkos, S., Kamo, S.L., Hickman, A.H., and Corfu, F., 2009, Measurement of SIMS Instrumental Mass Fractionation of Pb Isotopes During Zircon Dating: Geostandards and Geoanalytical Research, v. 33, no. 2, p. 145–168.

Trueb, L.F., and Butterman, W.C., 1969, Carbonado: A microstructural study: American Mineralogist, v. 54, p. 412–425.

Trueb, L.F., and de Wys, E., 1971, Carbon from Ubangi- A microstructural study: American Mineralogist, v. 56, p. 1252–1268.

Williams, I.S., 1998, U-Th-Pb Geochronology by Ion Microprobe, *in* McKibben, M.A., Shanks III, W.C., and Ridley, W.I. eds., Applications of microanalytical techniques to understanding mineralizing processes, Reviews in Economic Geology, p. 1–35.

Wilson, N.C., MacRae, C.M., Torpy, A., Davidson, C.J., and Vicenzi, E.P., 2012, Hyperspectral Cathodoluminescence Examination of Defects in a Carbonado Diamond: Microscopy and Microanalysis, v. 18, no. 6, p. 1303–1312.

Tables

Table DR1: Compositions of eight florencite grains and a lanthanum phosphate grain. These minerals were found in the pores of carbonados CAR 2 and CAR 16. Oxides below the detection limit denoted as "b", those not measured are denoted as "-". All measurements were performed by EDS using a JEOL 6400 analytical SEM or a CAMECA "microbeam" electron probe.
Table DR2: Pb isotopic compositions of lead in florencite. Measurements were done using the SHRIMP II ion microprobe.
Table DR3: Laser ICPMS U-Pb geochronology data for Rio Cachorrinho zircons.
Table DR4: Laser ICPMS U-Pb geochronology data for zircons from green quartzite clasts from the Lavras conglomerate of the Tombador Formation.
Table DR5: Laser ICPMS U-Pb geochronology data for zircons from the green quartzites of the Rio do Ouro Formation, Jacobina sequence.
Table DR6: SHRIMP U-Pb geochronology data for zircons from green quartzite clasts from Lavras conglomerate of the Tombador Formation.
Table DR7: SHRIMP U-Pb geochronology data for zircons from the green quartzites of the Rio do Ouro Formation, Jacobina sequence.
Tables are provided in a separate excel file.

Figures:

Figure DR1: Geologic map of the Lencois region, showing the location of the Rio Cachorrinho and it's associated drainage area. This stream was chosen for sampling due to the small catchment with limited lithology.

Figure DR2. Reflected light photomicrographs of 8 selected carbonado grains showing a range of microstructural textures. a: CAR 17; b: RE3; c: CAR16; d: CAR24; e: RG1; f: B1; g: CAR1; h: RF7. All scale bars are 0.2 mm.

Figure DR3: Multispectral SEM image of carbonado CAR25. The pores in this carbonado show orange CL around their rims, which contrasts with the green response from the rest of the carbonado. pore walls are quenched, and bull's eye halos are present. Images courtesy of the Smithsonian Institution (Suitland MD, USA).

Figure DR4: Multispectral SEM image of Brazilian carbonado RG6. This image shows the CL around numerous pores, with some showing slight brightening, many showing darkening, and a few showing completely quenched halos. Images courtesy of the Smithsonian Institution (Suitland MD, USA).

Figure DR5: A luminoscope photograph of carbonado CAR 17. Virtually all the pores in this sample are surrounded by large, completely quenched halos. Several bull's eye halos are also visible. Field of view is approximately 1.2 mm.

Figure DR6: Multispectral SEM image of Brazilian carbonado L3. This image shows the range of CL colors emitted by this carbonado. A variety of euhedral to subhedral grains are imbedded in a fine-grained matrix. Areas near
pores are CL dark due to epigenetic radiation damage, and bull's eye halos are present. Images courtesy of the Smithsonian Institution (Suitland MD, USA).

Figure DR7: A multispectral SEM CL image of carbonado L-5, collected near Lençois, Bahia state, Brazil. This carbonado has extremely large grains, and the entire image is one diamond crystal. The polygonal shapes with blue CL response are typical of primary CL features seen in monocrystalline diamond. Images courtesy of the Smithsonian Institution (Suitland MD, USA).

Figure DR8: Exterior photograph of carbonado CAR 1. This picture, taken with a binocular microscope, shows some of the unusual surface textures found on many carbonados. Scale bar gradations are 0.5 mm. The left side of the picture shows the glassy black surface texture, while the right side shows an uneven, reddish-brown surface that has been described as a "cantaloupe-like" texture (Haggerty, 1998).

Figure DR9: Exterior photograph of carbonado CAR 24. The scale bar has half mm gradations. This picture shows the slightly rounded, frosted end of this carbonado. This texture is probably caused by wear in a high energy sedimentary environment in which carbonado is found. However, as is shown here, the pores in this surface exhibit a shiny, 'glassy', texture and black color similar to part of the exterior of CAR 1, as is shown in Figure DR8. Most of them are also partially filled with a white pore mineral.

Figure DR10: Tera-Wasserberg Concordia plot of Rio Cachorrinho detrital zircons. Data point error ellipses are 68.3% confidence intervals

Figure DR11: Rio Cachorrinho detrital zircon age frequency plot.

Figure DR12: Tera-Wasserberg Concordia plot of zircons from the green fuchsitic clasts of the Tombador Formaiton conglomerates. Red is SHRIMP data, yellow is laser ICPMS data.

Figure DR13: Tera-Wasserberg Concordia plot of zircons from the Jacobina group quartzites (Rio do Ouro Fm). Red is SHRIMP data, yellow is laser ICPMS data.

Figure DR1

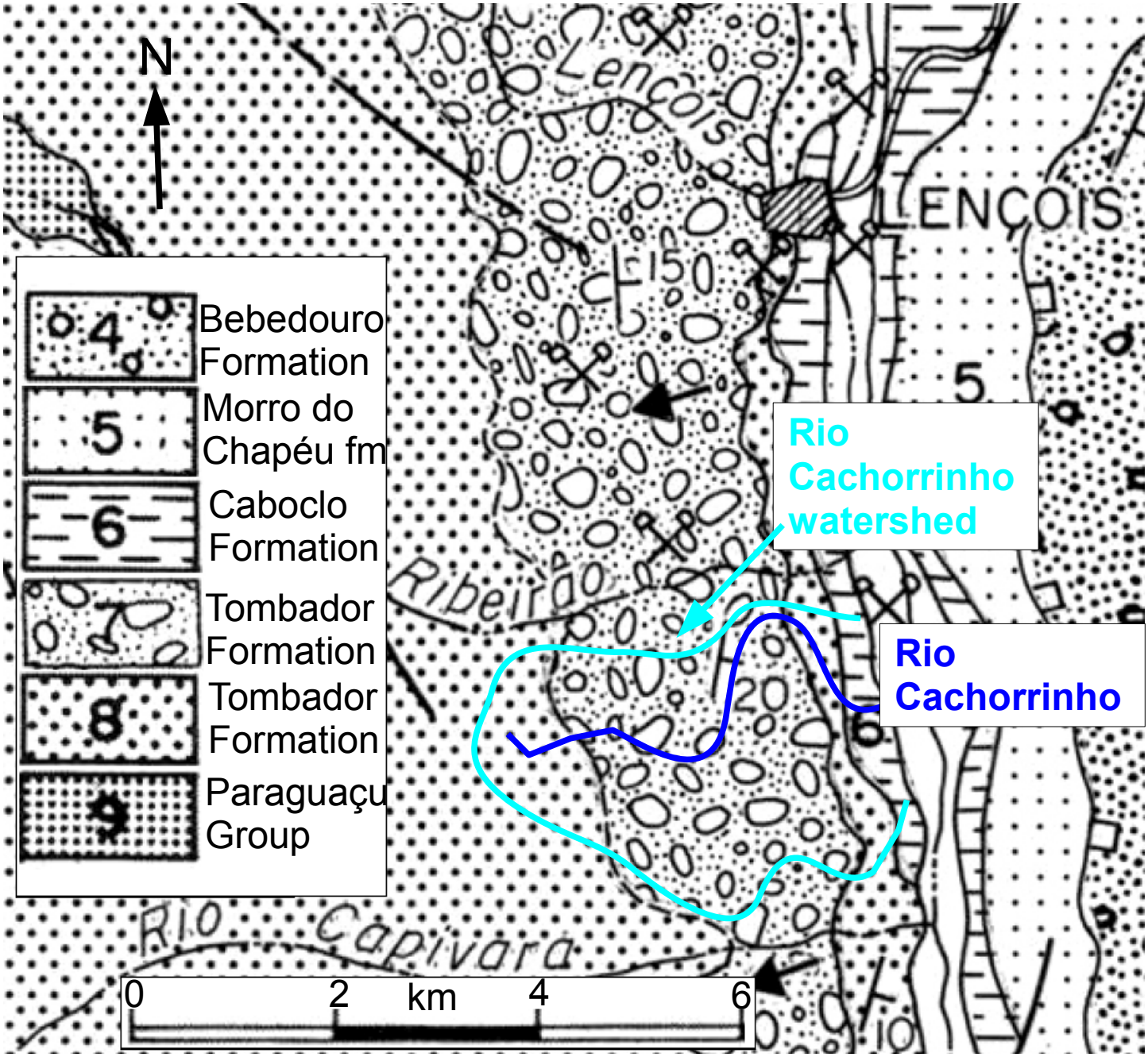
N
Lençois
LENÇOIS
150
5
Rio
Cachorrinho
watershed
Ribeirão
Rio
Cachorrinho
20
6
10
Rio Capivara
0
2
km
4
6
4
Bebedouro
Formation
5
Morro do
Chapéu fm
6
Caboclo
Formation
7
Tombador
Formation
8
Tombador
Formation
9
Paraguaçu
Group

Figure DR2

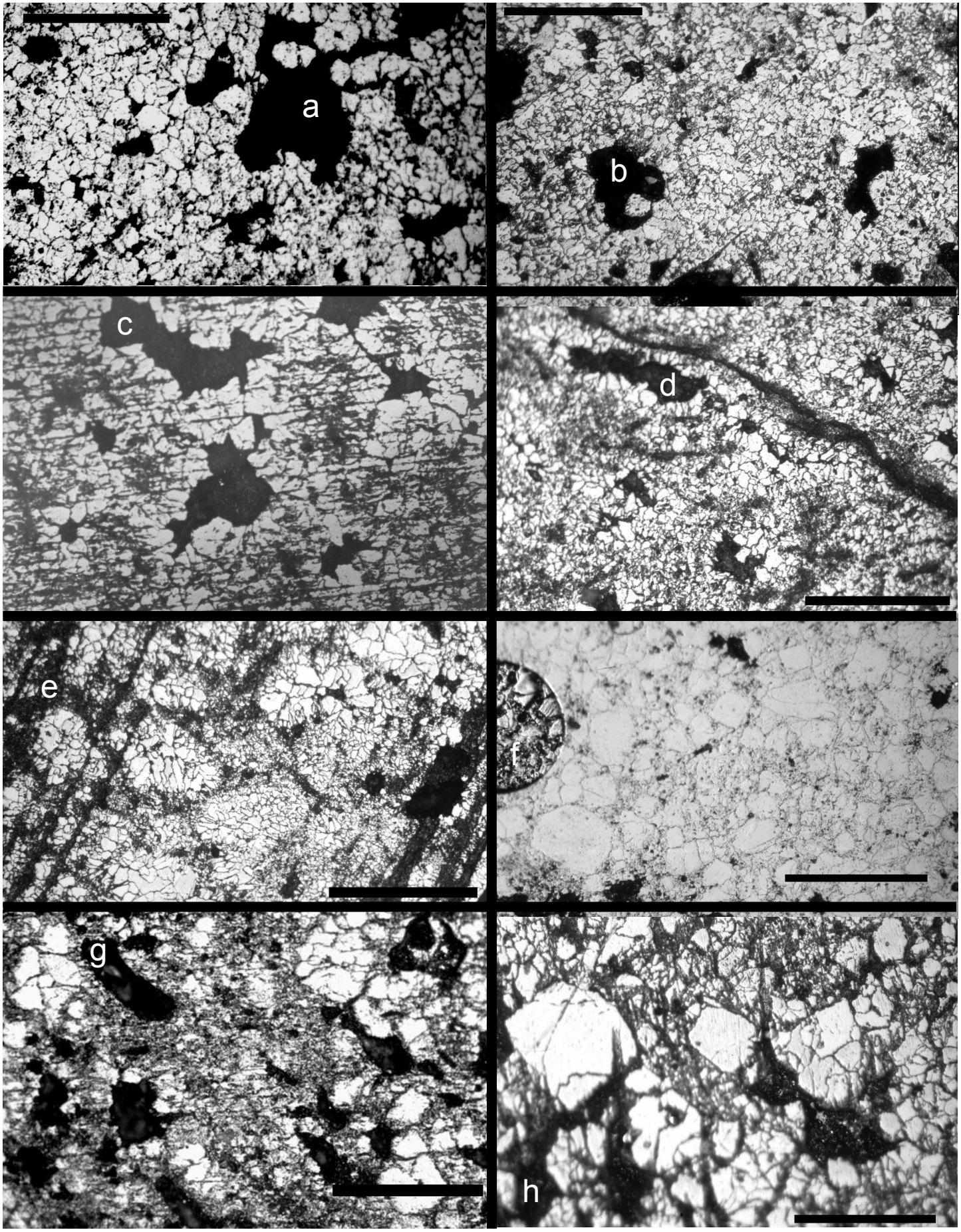

Figure DR3

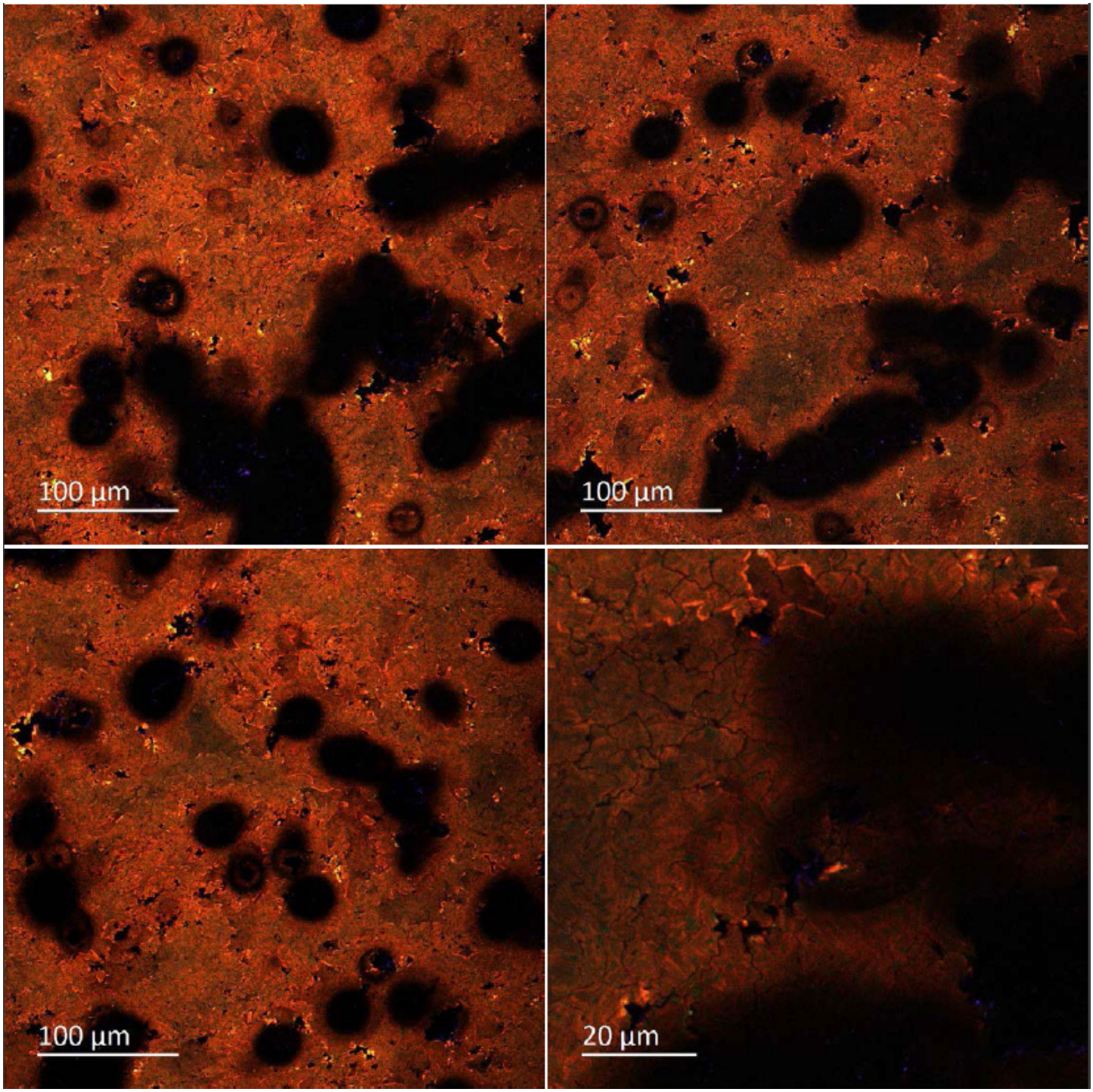

Figure DR4

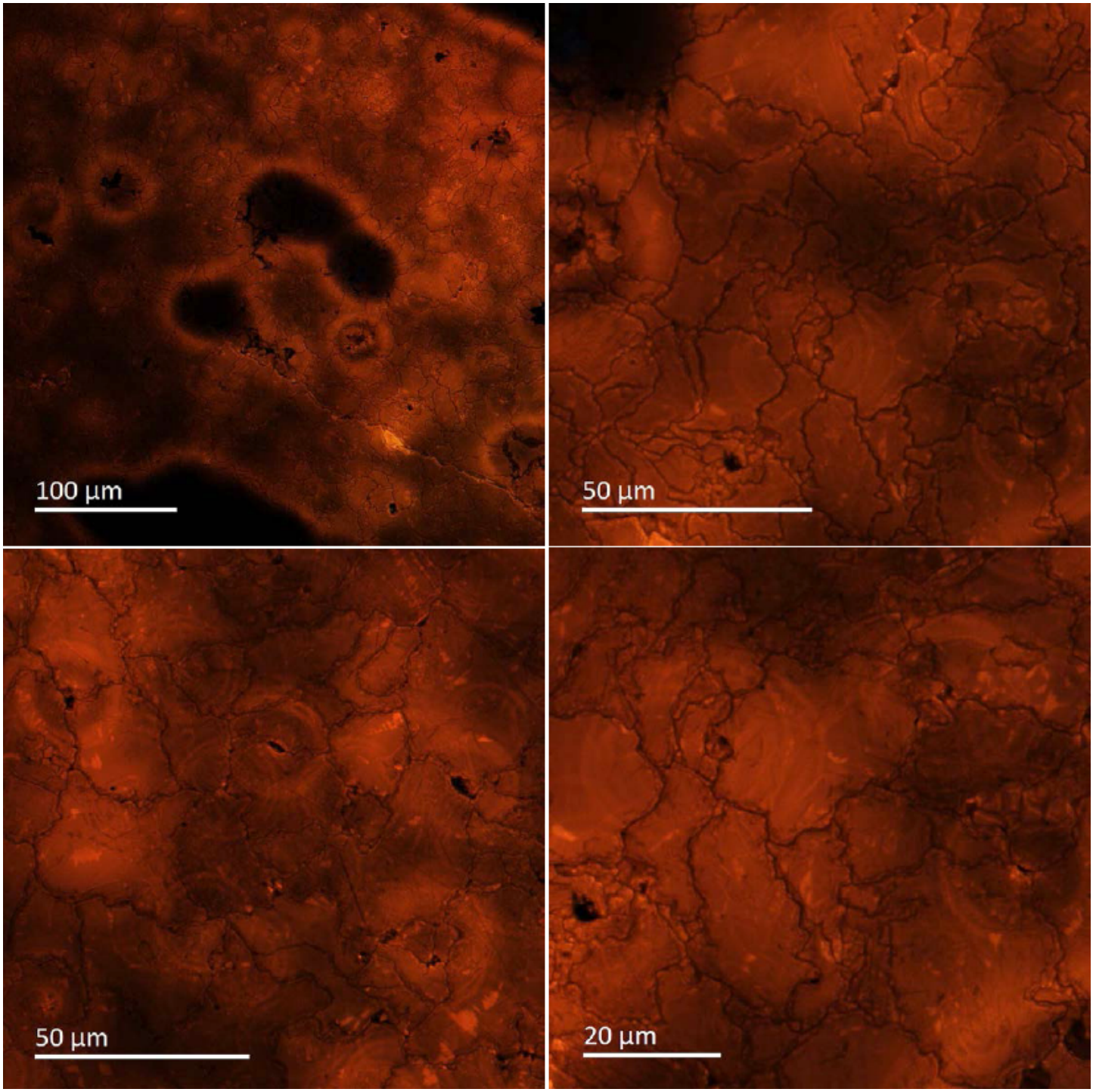

Figure DR5

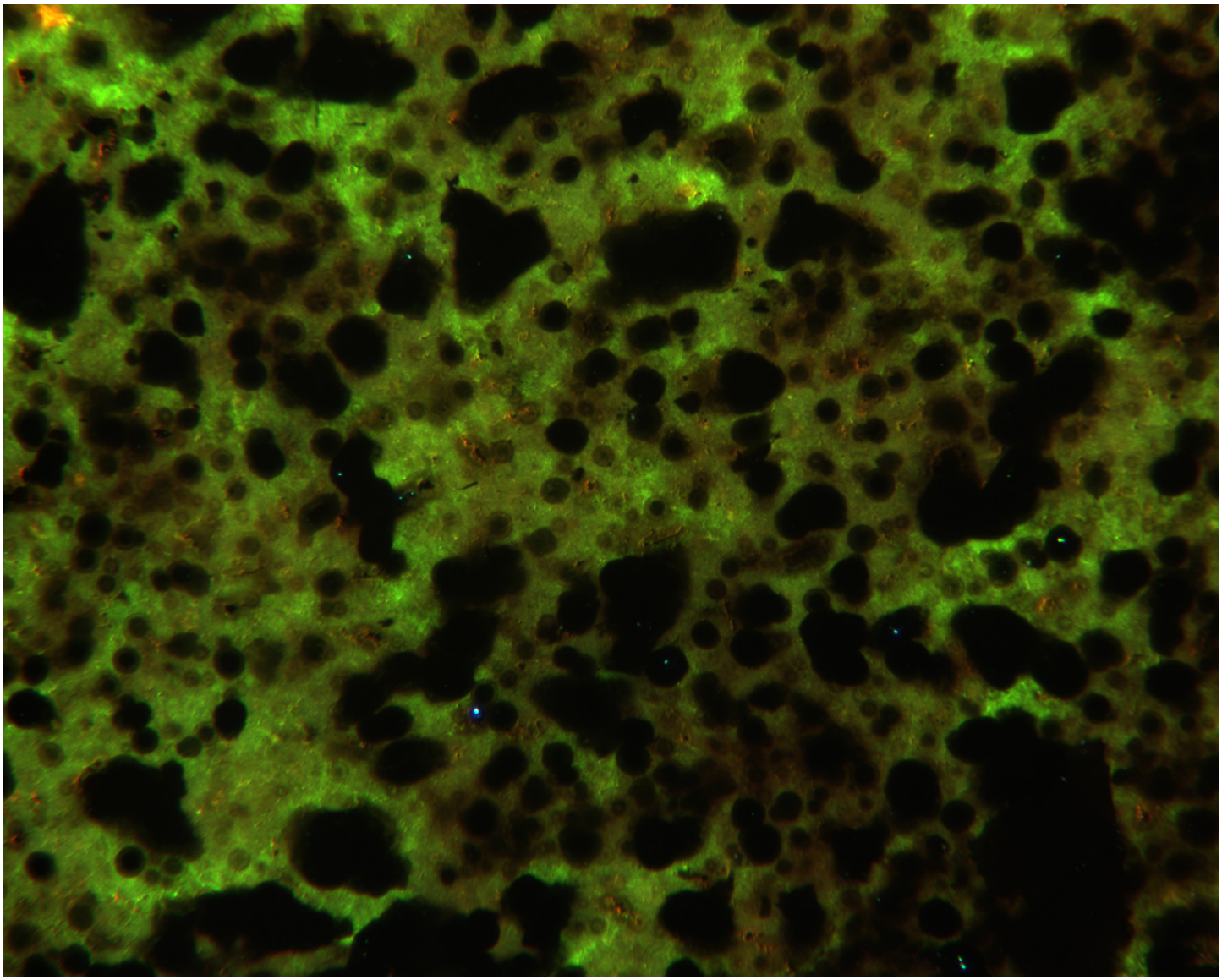

Figure DR6

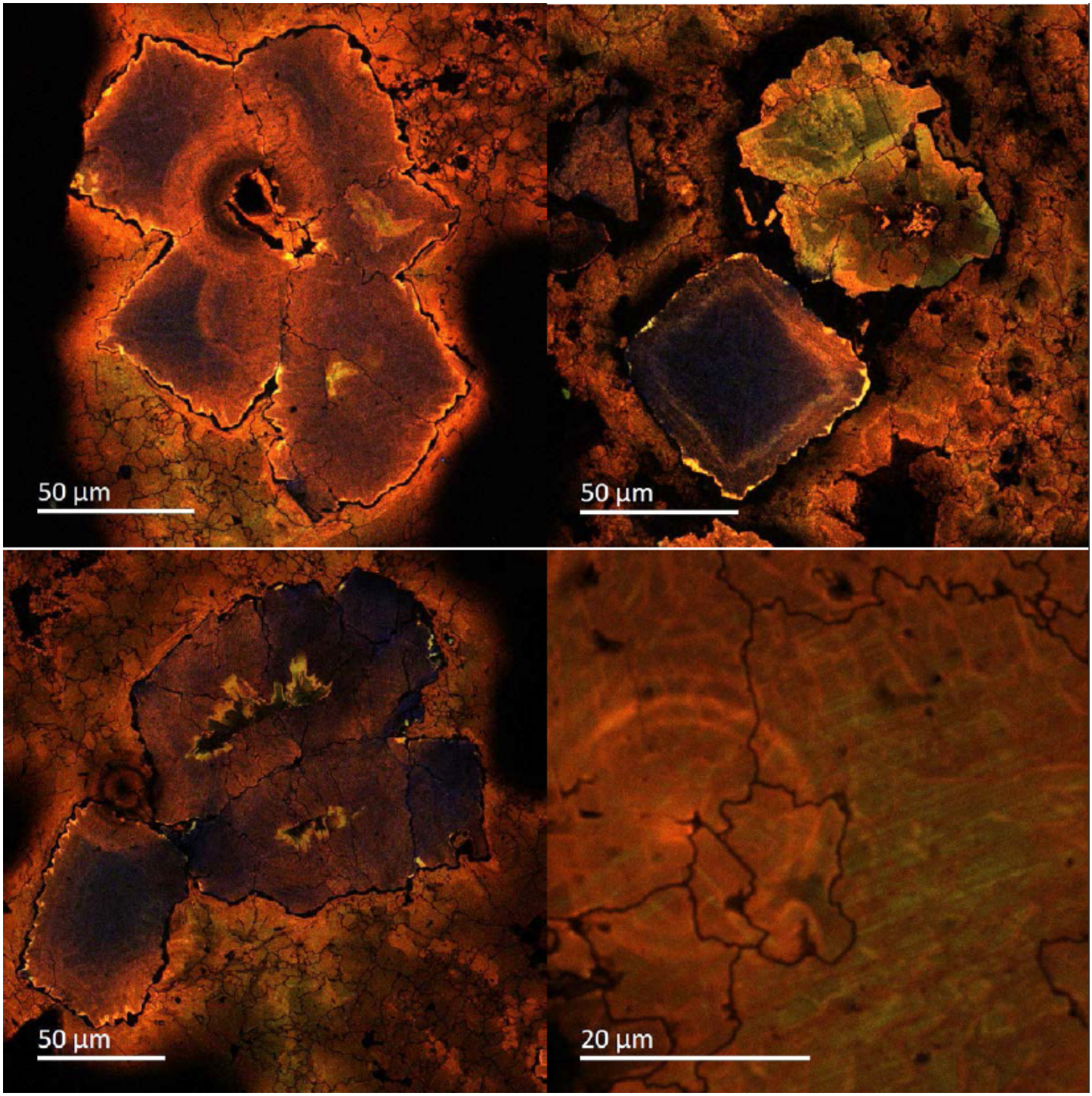

Figure DR7

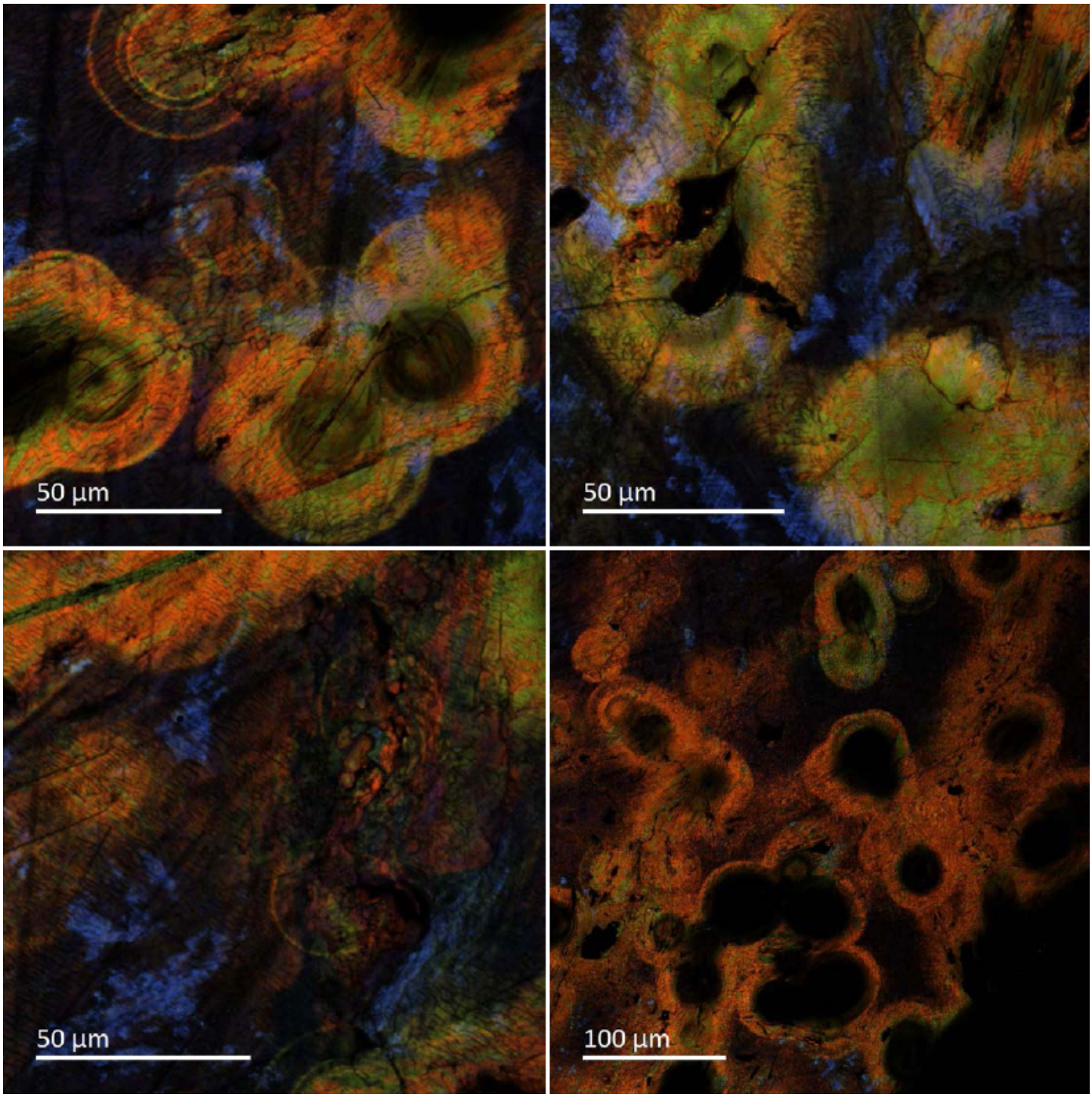

Figure DR8

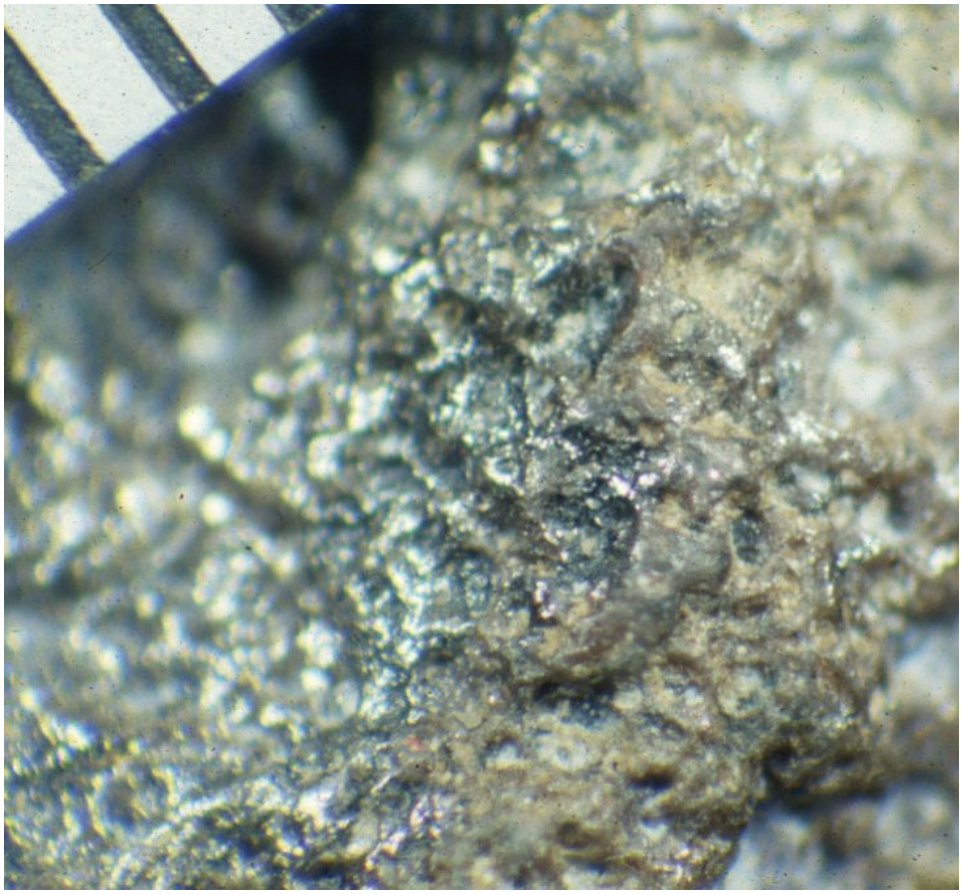

Figure DR9

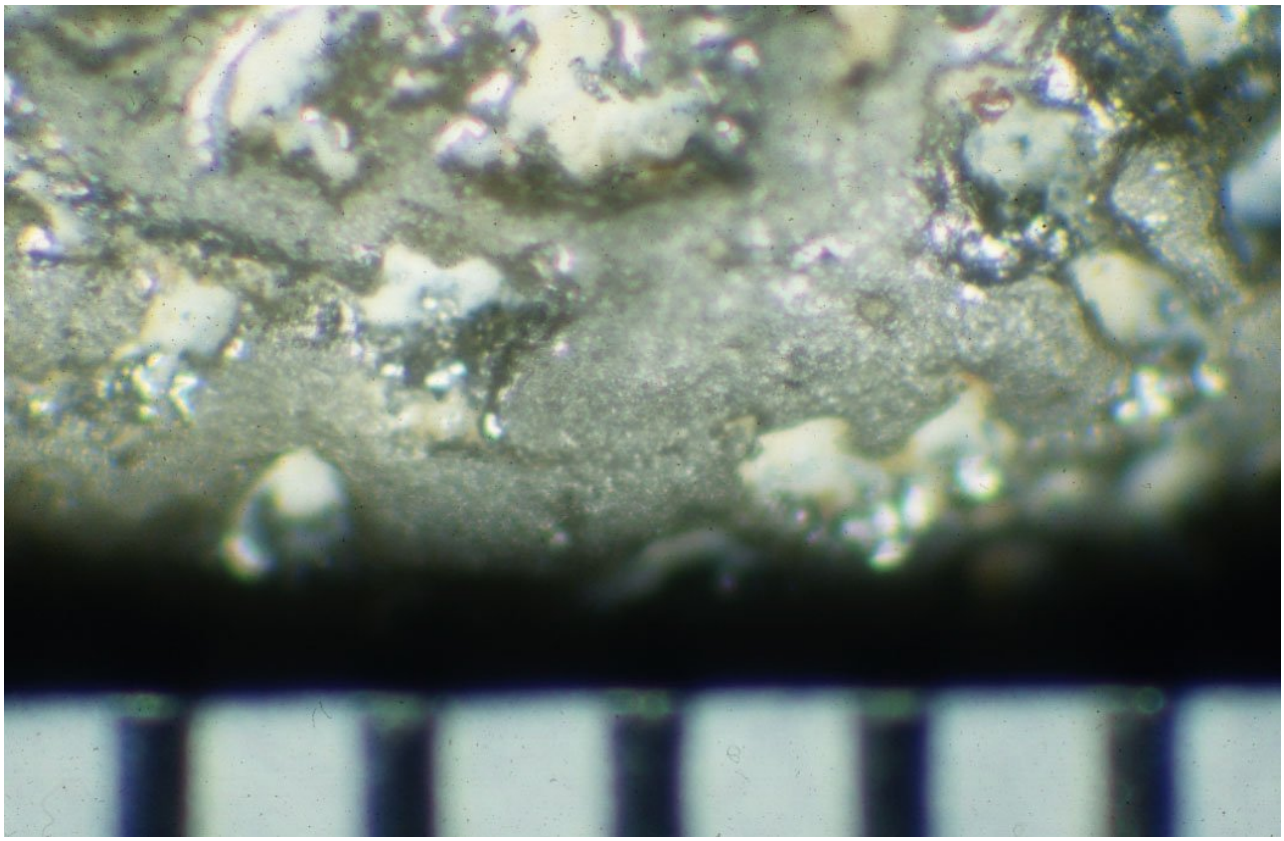

Figure DR10

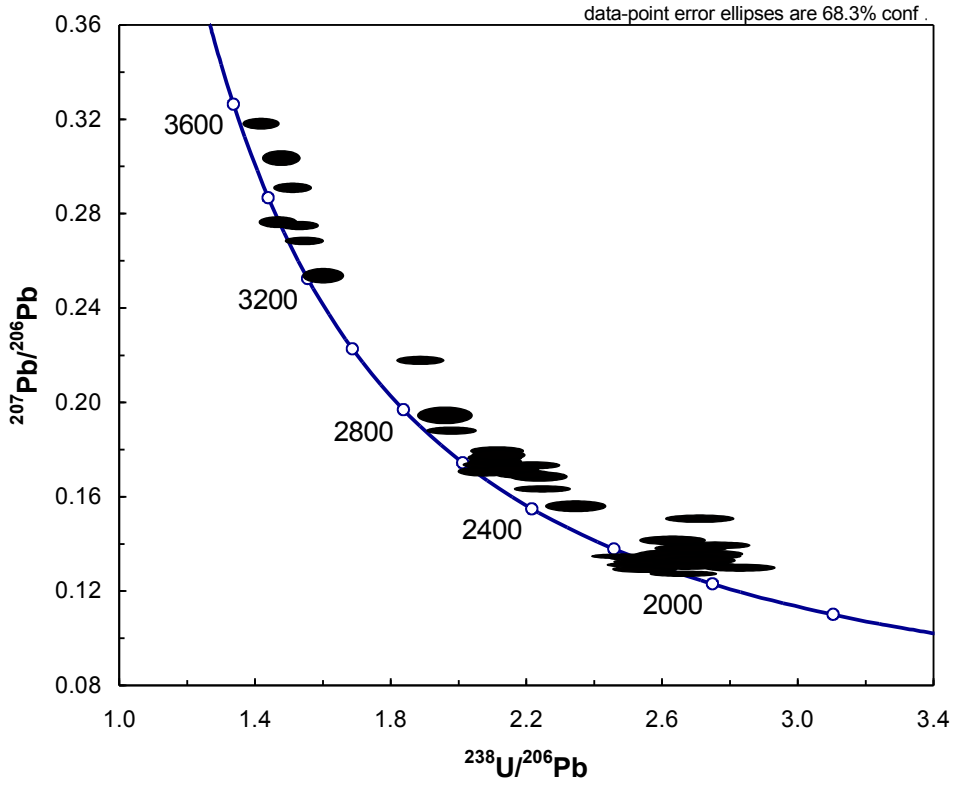
data-point error ellipses are 68.3% conf .
0.36
0.32
0.28
0.24
0.20
0.16
0.12
0.08
3600
3200
2800
2400
2000
1.0
1.4
1.8
2.2
2.6
3.0
3.4
207Pb/206Pb
238U/206Pb

Figure DR11

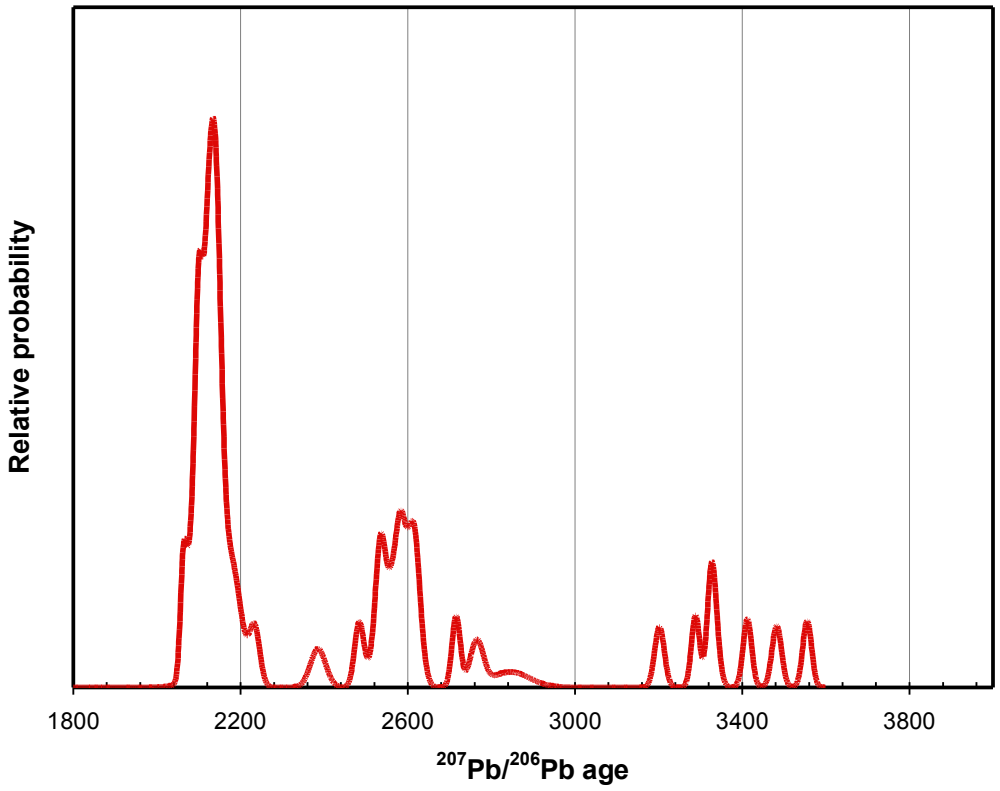
Relative probability
1800
2200
2600
3000
3400
3800
$^{207}Pb/^{206}Pb$ age

Figure DR12

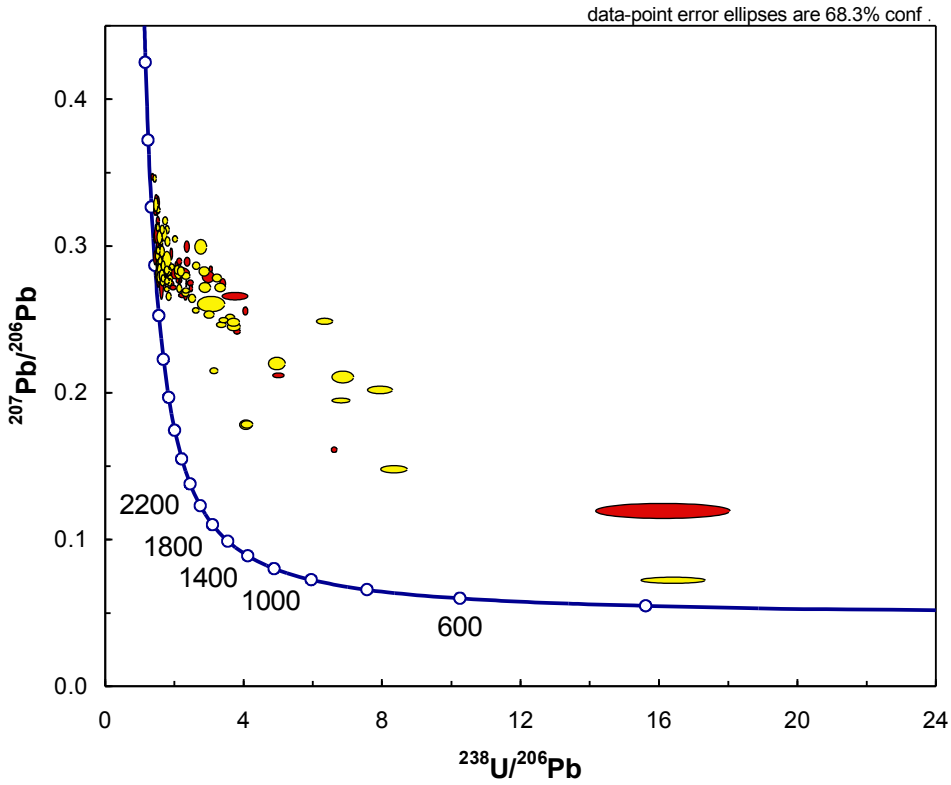
data-point error ellipses are 68.3% conf .
0.4
0.3
0.2
0.1
0.0
$^{207}Pb/^{206}Pb$
2200
1800
1400
1000
600
0
4
8
12
16
20
24
$^{238}U/^{206}Pb$

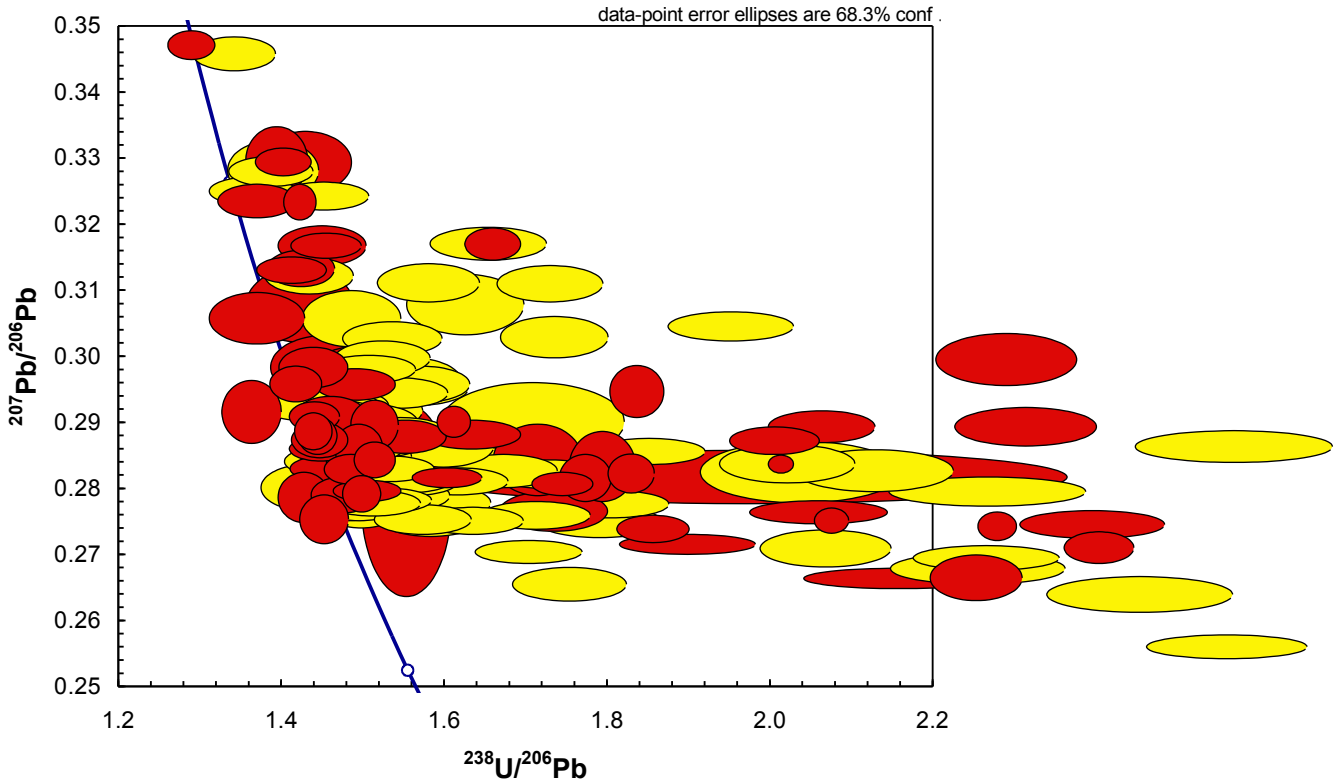
data-point error ellipses are 68.3% conf .
0.35
0.34
0.33
0.32
0.31
0.30
0.29
0.28
0.27
0.26
0.25
$^{207}Pb/^{206}Pb$
1.2
1.4
1.6
1.8
2.0
2.2
$^{238}U/^{206}Pb$

Figure
DR13

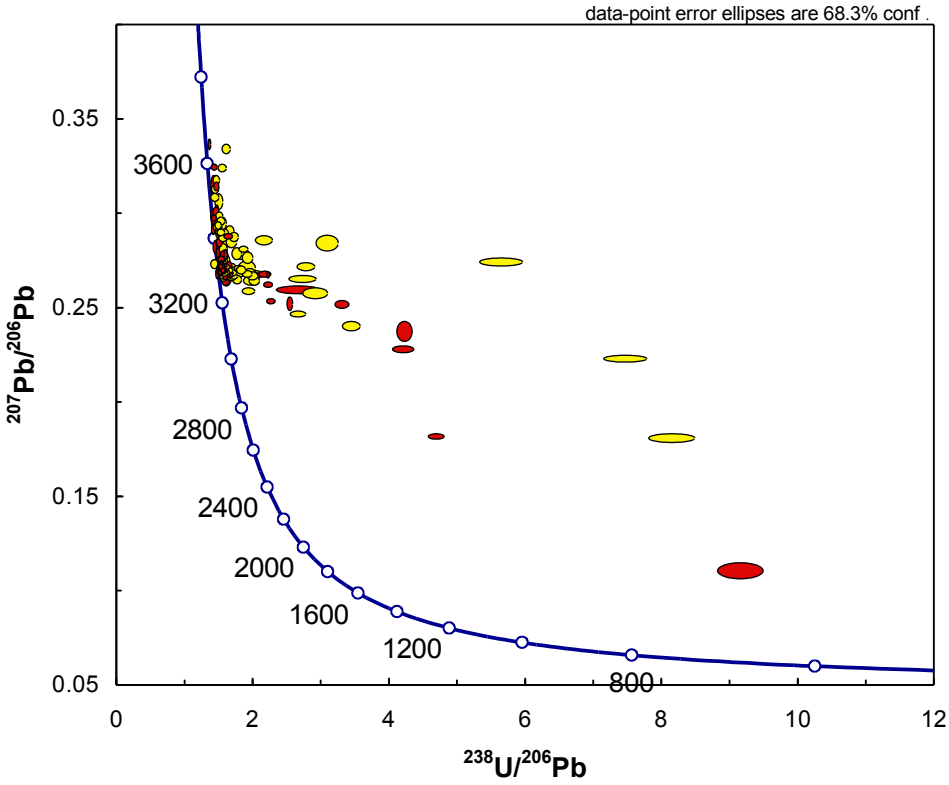
data-point error ellipses are 68.3% conf .
0.35
0.25
0.15
0.05
3600
3200
2800
2400
2000
1600
1200
800
0
2
4
6
8
10
12
207Pb/206Pb
238U/206Pb

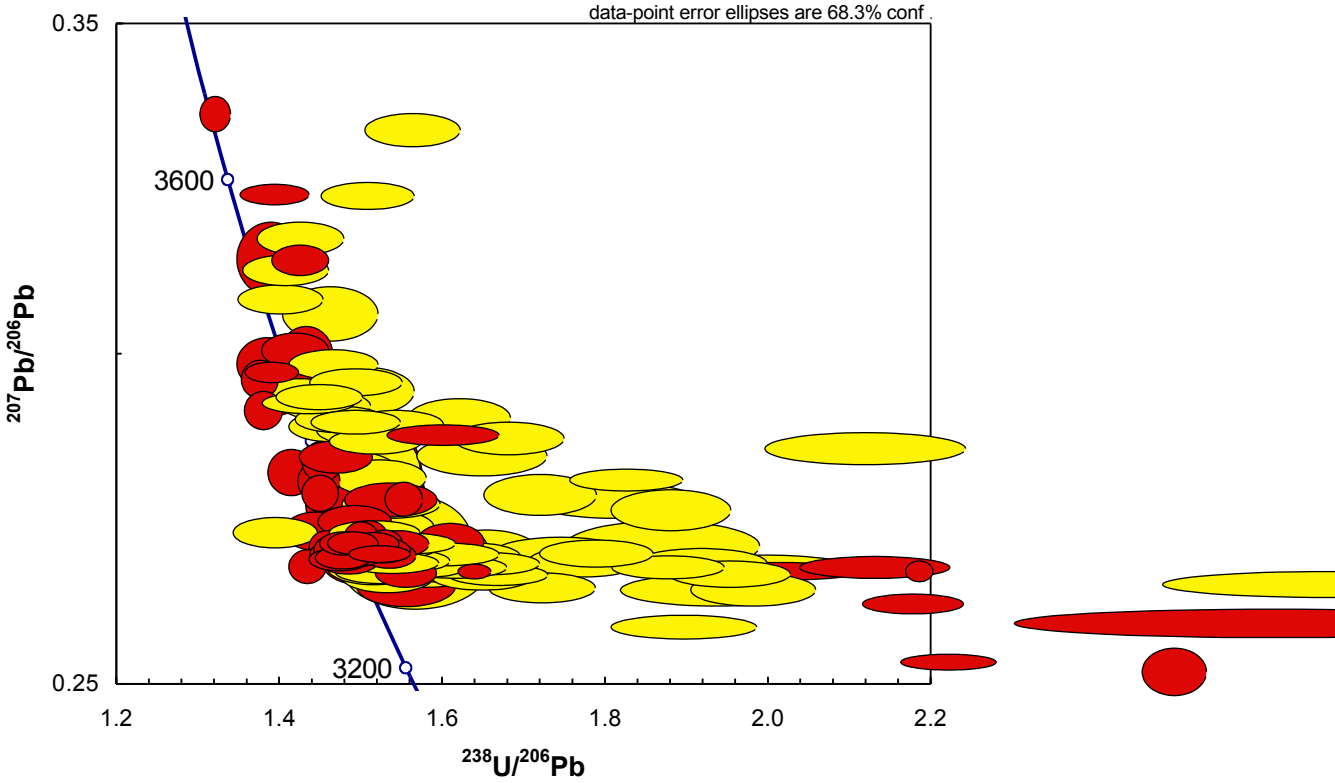
data-point error ellipses are 68.3% conf .
0.35
0.25
3600
3200
1.2
1.4
1.6
1.8
2.0
2.2
207Pb/206Pb
238U/206Pb